




# Electronic structure and magnetic tendencies of trilayer $\text{La}_4\text{Ni}_3\text{O}_{10}$ under pressure: Structural transition, molecular orbitals, and layer differentiation

Harrison LaBollita <sup>1,\*</sup>, Jesse Kapeghian <sup>1</sup>, Michael R. Norman <sup>2</sup>, and Antia S. Botana<sup>1</sup>

<sup>1</sup>*Department of Physics, Arizona State University, Tempe, Arizona 85287, USA*

<sup>2</sup>*Materials Science Division, Argonne National Laboratory, Lemont, Illinois 60439, USA*



(Received 15 February 2024; revised 12 April 2024; accepted 26 April 2024; published 15 May 2024)

Motivated by the recent observation of superconductivity in the pressurized trilayer Ruddlesden-Popper (RP) nickelate  $\text{La}_4\text{Ni}_3\text{O}_{10}$ , we explore its structural, electronic, and magnetic properties as a function of hydrostatic pressure from first-principles calculations. We find that an orthorhombic (monoclinic)-to-tetragonal transition under pressure takes place concomitantly with the onset of superconductivity. The electronic structure of  $\text{La}_4\text{Ni}_3\text{O}_{10}$  can be understood using a molecular trimer basis wherein  $n$  molecular subbands arise as the  $d_{z^2}$  orbitals hybridize strongly along the  $c$  axis within the trilayer. The magnetic tendencies indicate that the ground state at ambient pressure is formed by nonmagnetic inner planes and stripe-ordered outer planes that are antiferromagnetically coupled along the  $c$  axis, resulting in an unusual  $\uparrow, 0, \downarrow$  stacking that is consistent with the spin density wave model previously suggested by neutron diffraction. Such a state is destabilized at the pressure where superconductivity arises. Despite the presence of  $d_{z^2}$  states at the Fermi level, the  $d_{x^2-y^2}$  orbitals also play a key role in the electronic structure of  $\text{La}_4\text{Ni}_3\text{O}_{10}$ . This active role of the  $d_{x^2-y^2}$  states in the low-energy physics of the trilayer RP nickelate, together with the distinct electronic behavior of the inner and outer planes, resembles the physics of multilayer cuprates.

DOI: [10.1103/PhysRevB.109.195151](https://doi.org/10.1103/PhysRevB.109.195151)

## I. INTRODUCTION

Since the discovery of high-temperature superconductivity (HTS) in cuprates, identifying analogous materials that could help determine the essential components for HTS has posed a significant challenge in condensed matter physics [1]. Recently, superconductivity was discovered in the layered nickelate family  $R_{n+1}\text{Ni}_n\text{O}_{2n+2}$  ( $R$  = rare earth), providing a new perspective on this endeavor. Similar to the cuprates, these reduced layered nickelates have  $n$ - $\text{NiO}_2$  planes, and superconductivity in them emerges from a  $3d^{9-\delta}$  ( $\delta = 1/n \sim 0.2$ ) electron configuration on the Ni sites. The first superconducting member of the family was the infinite-layer ( $n = \infty$ ) material  $R\text{NiO}_2$  ( $R = \text{La}, \text{Pr}, \text{Nd}$ ), in which superconductivity with a maximum  $T_c \sim 15$  K arises upon hole doping [2–5]. Subsequently, superconductivity was also found in the quintuple-layer ( $n = 5$ ) compound  $\text{Nd}_6\text{Ni}_5\text{O}_{12}$ , which exhibits a similar  $T_c$  without the need for chemical doping [6]. This series of discoveries showed that akin to cuprates, the  $R_{n+1}\text{Ni}_n\text{O}_{2n+2}$  nickelate series represents a whole family of superconductors.

The field was recently reinvigorated after the discovery of superconductivity under pressure ( $\sim 14$  GPa) in bilayer  $\text{La}_3\text{Ni}_2\text{O}_7$  with a maximum  $T_c \sim 80$  K [7–9]. This material with an average  $\text{Ni}^{2.5+}$  ( $d^{7.5}$ ) is the  $n = 2$  member of the  $R_{n+1}\text{Ni}_n\text{O}_{3n+1}$  Ruddlesden-Popper (RP) phases, the parent compounds of the reduced layered  $R_{n+1}\text{Ni}_n\text{O}_{2n+2}$  family. Unlike reduced nickelates, the Ni atoms in these RP phases are coordinated by apical oxygens and have a nominal

electronic configuration for the Ni atoms of  $3d^{7+\delta}$  far from that of the cuprates. The discovery of superconductivity in this material ignited an explosion of experimental [10–12] and theoretical [13–37] work. Further, as with the reduced layered nickelate family, the extension of superconductivity to other members of the parent  $R_{n+1}\text{Ni}_n\text{O}_{3n+1}$  RP compounds has also been perceived as a crucial problem to be tackled. Very recently, superconducting signatures in the trilayer ( $n = 3$ ) RP nickelate  $\text{La}_4\text{Ni}_3\text{O}_{10}$  under pressure were also experimentally reported with  $T_c \sim 30$  K at pressures  $\sim 30$  GPa [38–40]. At ambient pressure, this material exhibits a metal-to-metal transition that results from an incommensurate density wave with both charge and magnetic character [41]. The discovery of superconductivity under pressure in the trilayer RP nickelate unlocked the  $R_{n+1}\text{Ni}_n\text{O}_{3n+1}$  series as a new family of superconducting nickelates.

For an emerging novel class of superconductors, it is crucial to find the analogies and differences among the members of the family. Here, using first-principles calculations, we analyze the structural, electronic, and magnetic properties of the trilayer RP nickelate  $\text{La}_4\text{Ni}_3\text{O}_{10}$  and contrast them with those of the bilayer material  $\text{La}_3\text{Ni}_2\text{O}_7$ . We find that in both materials, an orthorhombic (monoclinic)-to-tetragonal transition under pressure takes place that is concomitant with the onset of superconductivity. The electronic structure of  $\text{La}_4\text{Ni}_3\text{O}_{10}$  can be understood using a quantum-coupled unit—a molecular trimer basis—for the trilayer wherein  $n$  molecular subbands (bonding-nonbonding-antibonding) arise as the  $d_{z^2}$  orbitals hybridize strongly along the  $c$  axis. A similar picture has been proposed for  $\text{La}_3\text{Ni}_2\text{O}_7$  [13,42]. Our spin-polarized calculations indicate that the ground state of  $\text{La}_4\text{Ni}_3\text{O}_{10}$  at ambient pressure is formed by stripe-ordered

\*hlabolli@asu.edu

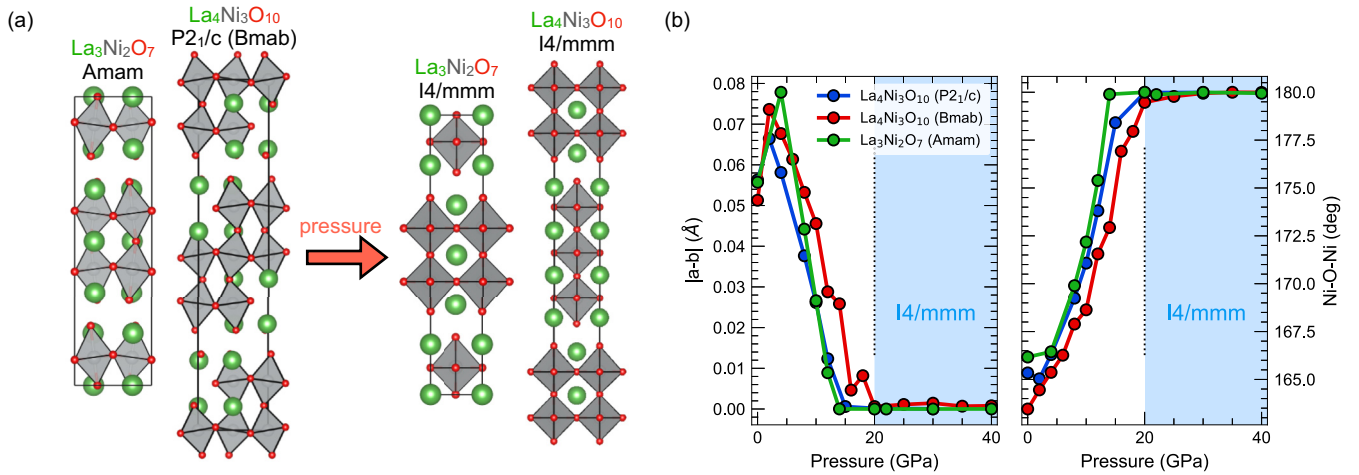


FIG. 1. “Tetragonalization” of the crystal structure of  $\text{La}_{n+1}\text{Ni}_n\text{O}_{3n+1}$  ( $n = 2, 3$ ) under pressure. (a) The ambient pressure structures for  $\text{La}_3\text{Ni}_2\text{O}_7$  ( $n = 2$ ; orthorhombic  $Amam$  crystal setting) and  $\text{La}_4\text{Ni}_3\text{O}_{10}$  ( $n = 3$ ; orthorhombic or monoclinic crystal settings) transform to tetragonal ( $I4/mmm$ ) structures under pressure. Green, gray, and red spheres denote the La, Ni, and O atoms, respectively. (b) Structural data capturing the structural transition with pressure: absolute difference  $|a - b|$  of the in-plane lattice constants (left) and apical Ni-O-Ni bond angle (right). At ambient pressure, the lattice constants used are the experimentally determined ones.

magnetic outer layers (coupled antiferromagnetically along the  $c$  axis) and nonmagnetic inner layers, consistent with the spin density wave model suggested by neutron diffraction data [11]. Such a state is destabilized at the pressures at which superconductivity has been observed. Importantly, as we found for  $\text{La}_3\text{Ni}_2\text{O}_7$  [42], the  $d_{x^2-y^2}$  orbitals play an active role in the electronic structure of the trilayer RP nickelate under pressure, which, together with the distinct behavior of the inner and outer layers, bears similarities to (multilayer) cuprates [43].

## II. METHODS

We used density-functional theory (DFT)-based calculations to investigate the structural properties, electronic structure, and magnetic tendencies of  $\text{La}_4\text{Ni}_3\text{O}_{10}$  under pressures up to 30 GPa [44,45]. The  $\text{La}_4\text{Ni}_3\text{O}_{10}$  structural data in the monoclinic (orthorhombic) and tetragonal settings were taken from Refs. [46,47], respectively. Structural optimizations of the crystal structure (unit cell and internal coordinates) were performed with the plane-wave pseudopotential-based DFT code VASP [48–50] within the generalized gradient approximation (GGA) [51] in the nonmagnetic state. For the ambient pressure structures, only the internal coordinates were optimized. The number of plane waves in the basis was set by an energy cutoff of 520 eV. The integration in reciprocal space was carried out on an  $8 \times 8 \times 2$  Monkhorst-Pack  $k$ -point grid. The internal forces on each atom were converged to  $10^{-6}$  eV/Å. Phonon calculations were performed using the frozen-phonon method as implemented in PHONOPY [52] interfaced with VASP for  $2 \times 2 \times 1$  supercells of the monoclinic ( $P2_1/c$ ) and tetragonal ( $I4/mmm$ ) crystal structures.

The electronic structure for each optimized crystal structure was subsequently calculated using the all-electron, full-potential DFT code WIEN2K [53]. The Perdew-Burke-Ernzerhof version of the GGA [51] was utilized for the exchange-correlation functional. To explore the magnetic tendencies, electronic correlation effects were included using an

on-site Coulomb repulsion  $U$  for the localized Ni ( $3d$ ) states. The around mean field (AMF) approach was employed for the double-counting correction [54]. The choice of AMF has been shown in previous work to give a reliable comparison to experiments in other layered nickelates [55–59] (as we showed in previous work [42], for  $\text{La}_3\text{Ni}_2\text{O}_7$  the energetics within the fully localized limit scheme are qualitatively similar to the AMF scheme). We used a range of Hubbard  $U$  values from 2 to 5 eV, while the Hund’s coupling  $J_H$  was fixed to the typical value of 0.7 eV for transition-metal  $3d$  electrons.  $RK_{\text{max}} = 7$  was used. Muffin-tin radii (in atomic units) of 2.5, 1.95, and 1.67 for La, Ni, and O, respectively, were employed. Dense  $21 \times 21 \times 21$  ( $30 \times 29 \times 11$ )  $k$  grids for the  $I4/mmm$  ( $P2_1/c$ ) crystal setting were used. For the larger supercells used in some of the magnetic states we calculated,  $k$  grids with similar densities were employed. For computational details on the  $\text{La}_3\text{Ni}_2\text{O}_7$  calculations, we refer the reader to Ref. [42].

## III. RESULTS

### A. Tetragonalization and lattice dynamics of the crystal structure under pressure

Figure 1 shows the evolution of the structural parameters of the trilayer RP  $\text{La}_3\text{Ni}_2\text{O}_{10}$  with pressure (in comparison to those of bilayer  $\text{La}_3\text{Ni}_2\text{O}_7$ ). In  $\text{La}_3\text{Ni}_2\text{O}_7$ , initial x-ray diffraction (XRD) experiments under pressure revealed that superconductivity is accompanied by a structural transition from a low-symmetry  $Amam$  orthorhombic phase to a higher-symmetry (still orthorhombic)  $Fmmm$  phase with modest pressures ( $>10$ – $15$  GPa) [7]. This structural transition is characterized by the suppression of the tilts in the  $\text{NiO}_6$  octahedral cages. Using DFT calculations, we previously showed [42] (in agreement with other theory work [62]) that near  $\sim 15$  GPa, an orthorhombic-to-tetragonal ( $I4/mmm$ ) structural transition could occur instead [see Figs. 1(a) and 1(b)]. Importantly, this prediction of the “tetragonalization” of the structure under pressure is in agreement with recent low-temperature XRD

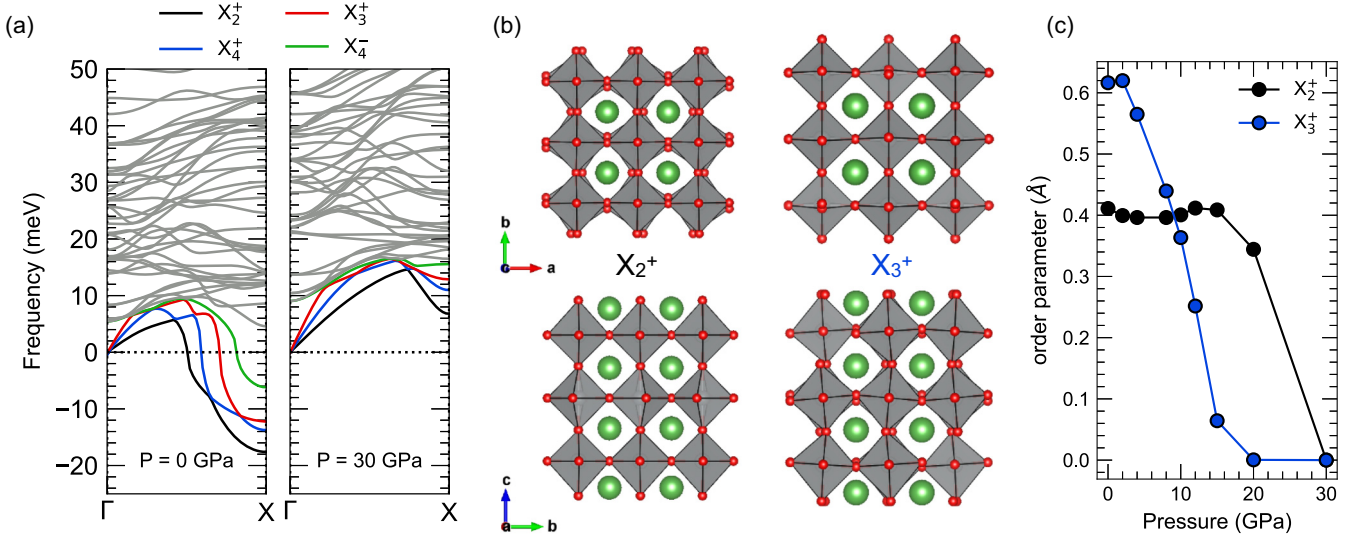


FIG. 2. Lattice dynamics of  $\text{La}_4\text{Ni}_3\text{O}_{10}$  under pressure. (a) Phonon dispersions at ambient pressure (left) and 30 GPa (right) for  $\text{La}_4\text{Ni}_3\text{O}_{10}$  in the tetragonal ( $I4/mmm$ ) crystal setting. Colors denote phonon branches corresponding to unstable modes. (b) Crystal distortions according to the  $X_2^+$  and  $X_3^+$  irreducible representations (irreps) of the  $I4/mmm$  space group in the  $ab$  (top) and  $bc$  (bottom) planes. (c) Order parameter amplitudes obtained from AMPLIMODES [60,61] for the  $X_2^+$  and  $X_3^+$  irreps relative to the ambient pressure tetragonal crystal structure.

experiments [12], which have confirmed that an  $I4/mmm$  phase arises in  $\text{La}_3\text{Ni}_2\text{O}_7$  at low temperatures ( $\sim 40$  K) when compressed to 19 GPa [63].

Analogous structural relaxations for  $\text{La}_4\text{Ni}_3\text{O}_{10}$  using either the monoclinic  $P2_1/c$  or orthorhombic  $Bmab$  crystal structure as a starting point [41,46,64,65] indicate an identical structural transition with pressure takes place in the trilayer material [see Figs. 1(a) and 1(b)], in agreement with other recent theoretical [37] and experimental [66] works. Near  $\sim 10$ –15 GPa, the structure of  $\text{La}_4\text{Ni}_3\text{O}_{10}$  tetragonalizes with the collapse of the in-plane lattice constants to the same value and the suppression of the octahedral tilts. The tetragonal structure can also be seen to become the more energetically favored structure with pressure when comparing the enthalpies of the low-symmetry ( $P2_1/c$ ) and high-symmetry ( $I4/mmm$ ) phases (see Fig. 6 in Appendix A).

To gain further insight into the lattice dynamics driving the transition towards a tetragonal structure in  $\text{La}_4\text{Ni}_3\text{O}_{10}$ , we calculate the evolution of the phonons with pressure in the high-symmetry tetragonal ( $I4/mmm$ ) setting (see Fig. 2). At ambient pressure we identify four unstable modes at the  $X$  point with the  $X_2^+$ ,  $X_4^+$ ,  $X_3^+$ , and  $X_4^-$  irreducible representations (irreps) of the  $I4/mmm$  space group [see Fig. 2(a)]. The  $X_2^+$  irrep corresponds to the distortion of the in-plane oxygens, while the  $X_3^+$ ,  $X_4^+$ , and  $X_4^-$  irreps correspond to the distortions of the apical oxygens in the  $\text{NiO}_6$  cage that are linked to the octahedral tilts [see Fig. 2(b)]. We find that these four unstable modes become quenched with pressure: Initially, the  $X_3^+$  mode associated with the  $\text{NiO}_6$  octahedral tilts is suppressed. Subsequently, the  $X_2^+$  mode corresponding to the in-plane distortion of the  $\text{NiO}_6$  octahedra is quenched [see Fig. 2(c), as well as further details on the phonon calculations in Fig. 6 in Appendix A]. Importantly, a symmetry mode analysis (obtained from AMPLIMODES [60,61]) reveals that the  $X_2^+$  and  $X_3^+$  distortions are the ones responsible for driving the transition between  $P2_1/c$  and  $I4/mmm$ . Overall, our results

indicate that at the pressure at which superconductivity onsets, the structures for both the bilayer and trilayer RP nickelates are tetragonal.

## B. Evolution of the electronic structure with pressure

We begin our analysis by examining the pressure-induced variations in the nonmagnetic electronic structure of  $\text{La}_4\text{Ni}_3\text{O}_{10}$ . A formal valence count for  $\text{La}_4\text{Ni}_3\text{O}_{10}$  renders an (average)  $\text{Ni}^{2.67+}$  ion corresponding to a  $d^{7.33}$  filling of the Ni ( $3d$ ) shell. Within each trilayer complex (three  $\text{NiO}_6$  layers), one has (on average) four electrons in the Ni  $e_g$  orbitals, while the Ni  $t_{2g}$  orbitals are completely filled. In order to clearly understand the band fillings in  $\text{La}_4\text{Ni}_3\text{O}_{10}$ , the site- and orbital-resolved band structures are shown in Figs. 3(a) and 3(b) for the ambient pressure  $P2_1/c$  phase and for the  $I4/mmm$  structure at 30 GPa, where we distinguish the Ni  $e_g$  ( $d_{z^2}$  and  $d_{x^2-y^2}$ ) orbital contributions from the inequivalent inner- and outer-layer Ni sites (note that, at ambient pressure, the electronic structure in the  $Bmab$  space group is equivalent to that of the  $P2_1/c$  phase, as shown in Fig. 7 in Appendix B). As expected, in the vicinity of the Fermi level, both the  $d_{x^2-y^2}$  and  $d_{z^2}$  bands are active and strongly hybridized. It should be noted that the  $d_{z^2}$  bands are filled quite differently for different Ni atoms in the structure. In contrast, no relevant distinction is observed for the filling of the  $d_{x^2-y^2}$  orbitals. These differences in filling are robust with pressure, and we explain their origin below.

### 1. Molecular orbitals

The different band occupations for the inner and outer Ni atoms can be understood using the differences in  $d_{z^2}$  filling in terms of “molecular subbands” [47,67]. In essence,  $n$  molecular subbands arise in the RP nickelates as the  $d_{z^2}$  orbitals hybridize strongly along the  $c$  axis, with the molecular picture being due to the natural quantum confinement within



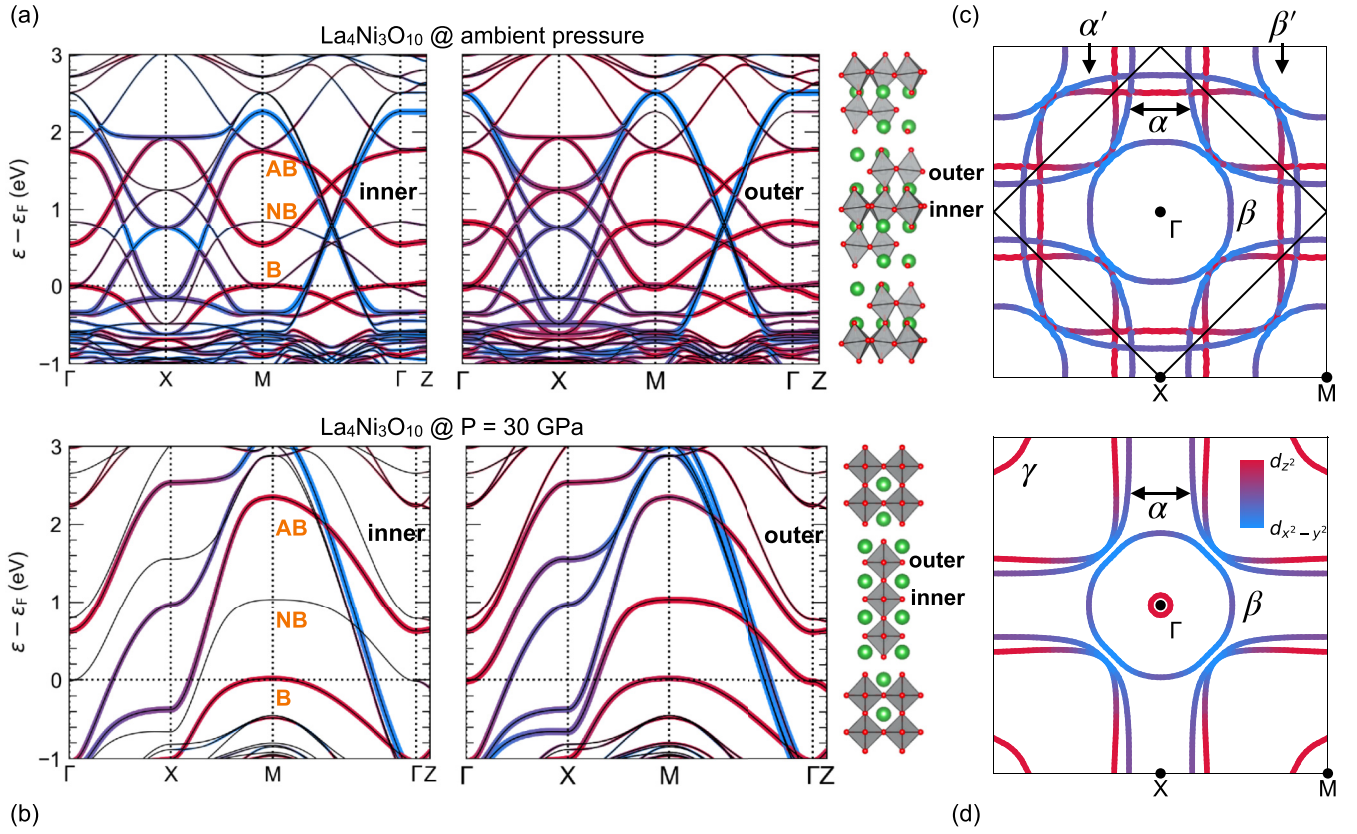


FIG. 3. Electronic structure of  $\text{La}_4\text{Ni}_3\text{O}_{10}$  at ambient pressure ( $P2_1/c$ , top row) and  $P = 30$  GPa ( $I4/mmm$ , bottom row). (a) and (b) Site- and orbital-resolved band structures along high-symmetry lines highlighting the Ni  $d_{z^2}$  (red) and Ni  $d_{x^2-y^2}$  (blue) orbital characters for the inner and outer inequivalent Ni sites for the ambient ( $P2_1/c$ ) and 30 GPa ( $I4/mmm$ ) phases, respectively. The Ni  $d_{z^2}$  bonding (B), nonbonding (NB), and antibonding (AB) bands are labeled. The corresponding crystal structure is shown to the right. (c) and (d) Corresponding Fermi surfaces for (a) and (b) in the  $k_z = 0$  plane with high-symmetry points and  $\alpha$ ,  $\beta$ , and  $\gamma$  sheets denoted ( $\alpha'$  and  $\beta'$  sheets are the back-folded versions of their unprimed counterparts).

the structure provided by the blocking slabs between successive Ni-O trilayers. As such, for the  $n = 3$  RP nickelate, for each Ni triple along the  $c$  axis with neighbors coupled by the hopping integral  $t_{\perp}$ , the corresponding eigenvalues and eigenvectors are [67]

$$\begin{aligned} \varepsilon_{z^2} &= 0, \pm \sqrt{2}t_{\perp}, \\ |\varepsilon_{z^2}\rangle &= \frac{1}{\sqrt{2}}(1, 0, -1), \frac{1}{2}(1, \mp\sqrt{2}, 1). \end{aligned} \quad (1)$$

The odd-symmetry nonbonding (NB) state ( $\varepsilon = 0$ ), which does not involve the inner Ni site, as shown by the corresponding eigenvector, is midway in energy between the even-symmetry bonding (B) and antibonding (AB) states. This clean picture of molecular orbitals explains the site- and orbital-resolved band structures we obtain. Importantly, this picture survives the application of pressure and the structural phase transition, but with increased splittings among the different molecular orbitals as pressure is applied.

The molecular orbital picture applies to the bilayer  $\text{La}_3\text{Ni}_2\text{O}_7$  material as well, but in that case, one has only two molecular subbands for the dimer forming a bonding-antibonding complex (and no effective difference between the two layers exists in terms of filling, in contrast to the trilayer

material). As a consequence of this splitting, in the bilayer nickelate [with an average Ni valence  $\text{Ni}^{2.5+}$  ( $d^{7.5}$ ), which corresponds to three electrons to be filled for each bilayer in the Ni  $e_g$  orbitals] two spin states are possible depending on how the three electrons fill the  $e_g$  states: (1) a low-spin (LS) state, wherein the  $d_{z^2}$  bonding orbital is doubly occupied but the antibonding state is empty, with the  $d_{x^2-y^2}$  orbitals being 1/4 filled, or (2) a high-spin (HS) state, in which the bonding  $d_{z^2}$  and  $d_{x^2-y^2}$  orbitals are all half filled (i.e., the majority spin channel is occupied) and the antibonding  $d_{z^2}$  state remains empty. We have found [42] that in  $\text{La}_3\text{Ni}_2\text{O}_7$  a low-spin state is favored in the high-pressure/superconducting phase, suggesting that the HS solution may be unfavorable for superconductivity in this material.

Returning to the trilayer nickelate case, with the above considerations for the  $d_{z^2}$  splittings (keeping in mind that the  $d_{x^2-y^2}$  states are equally occupied for all the Ni atoms), how can one fill up the available four electrons in the  $e_g$  levels? The different possible states are the following (see Fig. 4): (1) a nonmagnetic (NM) state, in which an electron occupies the majority and minority bonding  $d_{z^2}$  states and 1/3 of the majority and minority  $d_{x^2-y^2}$  bands, (2) a HS state, in which a  $d_{z^2}$  triplet (bonding-nonbonding-antibonding) is filled in addition to 1/3 of the majority  $d_{x^2-y^2}$  band, and (3) a LS state, in

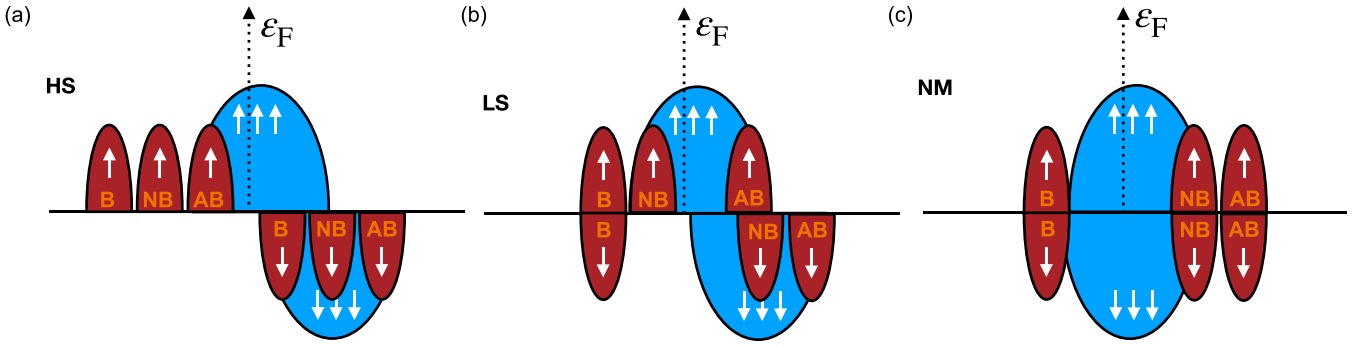


FIG. 4. Level scheme showing the possible spin states for the trilayer RP nickelate  $\text{La}_4\text{Ni}_3\text{O}_{10}$  using the molecular orbital picture for the Ni  $d_z^2$  states (three Ni atoms are represented; within each trilayer four electrons occupy the Ni  $e_g$  orbitals). The  $d_{x^2-y^2}$  states are depicted in blue; the  $d_z^2$  states are depicted in red. The bonding (B), nonbonding (NB), and antibonding (AB)  $d_z^2$  bands are labeled. (a) High spin (HS). (b) Low spin (LS). (c) Nonmagnetic (NM).

which the bonding  $d_z^2$  state is doubly occupied and 1/3 of the majority  $d_{x^2-y^2}$  band and the majority nonbonding  $d_z^2$  orbital are filled. We will return to the Ni spin states in  $\text{La}_4\text{Ni}_3\text{O}_{10}$  in Sec. C when describing its magnetic tendencies.

## 2. Fermi surface

To draw comparisons, we start by briefly describing the fermiology of the bilayer RP  $\text{La}_3\text{Ni}_2\text{O}_7$  (see Fig. 8 in Appendix C, where we use the notation of the angle-resolved photoelectron spectroscopy (ARPES) data for  $\text{La}_4\text{Ni}_3\text{O}_{10}$  [64] and refer to the different bands as  $\alpha$ ,  $\beta$ , and  $\gamma$ ). Its Fermi surface consists of one holelike sheet of dominant  $d_{x^2-y^2}$  character ( $\alpha$ ) centered at the corner of the tetragonal zone ( $M$ ), an electronlike sheet comprised of mixed  $e_g$  orbital character ( $\beta$ ) at  $\Gamma$ , and another hole pocket at  $M$  of dominant  $d_z^2$  character ( $\gamma$ ). The nature of these Fermi surface sheets does not significantly change with pressure. We note that the importance of the  $\gamma$  pocket for Cooper pairing (in  $s^\pm$  symmetry) was recently highlighted: if the  $\gamma$  pocket vanishes,  $s^\pm$  pairing is suppressed [26].

The fermiology of  $\text{La}_4\text{Ni}_3\text{O}_{10}$  is somewhat similar to that of its bilayer counterpart, with some relevant differences arising with pressure. At ambient pressure, the Fermi surface comprises two different types of sheets [see Fig. 3(c)]: two large hole pockets centered at the corner of the tetragonal Brillouin zone ( $\alpha$  band, split due to the interlayer hopping within the trilayer) and an electron pocket ( $\beta$ ) centered at  $\Gamma$ . The  $\alpha$  pocket has mixed  $e_g$  orbital characters, while the  $\beta$  pocket is predominantly  $d_{x^2-y^2}$  in character. The  $\alpha'$  and  $\beta'$  pockets are the back-folded versions of the  $\alpha$  and  $\beta$  pockets, respectively. We do not find the  $\gamma$  pocket obtained in ARPES (with mainly Ni  $d_z^2$  character) at ambient pressure at the GGA level unless the Fermi energy is shifted (as shown in Fig. 7 in Appendix B). It has been suggested [64] that the opening of a gap in the  $\gamma$ - $d_z^2$  band accompanies the charge density wave (CDW) formation at the metal-to-metal transition in  $\text{La}_4\text{Ni}_3\text{O}_{10}$ . We argue that this gap is instead due to back-folding (see Fig. 7 in Appendix B for the band structure of a  $\sqrt{2} \times \sqrt{2}$  cell of the  $I4/mmm$  structure, where the gap is closed).

If pressure is applied to  $\text{La}_4\text{Ni}_3\text{O}_{10}$ , the Fermi surface exhibits many of the same features ( $\alpha$  and  $\beta$  pockets) with the

addition of the  $\gamma$  pocket of dominant  $d_z^2$  character at the zone corner [see Fig. 3(d)]. We also find a small electron pocket emerging at  $\Gamma$  due to the nonbonding  $d_z^2$  band that broadens with pressure and crosses the Fermi level. As mentioned above, the importance of the  $\gamma$  pocket for Cooper pairing (in  $s^\pm$  symmetry) has been emphasized in bilayer nickelates [26]. With the inclusion of dynamical electronic correlations within single-site DFT+dynamical mean-field theory, the basic features of the fermiology that we describe remain the same under pressure [68–70].

## C. Magnetic tendencies with pressure

In order to find the magnetic ground state of  $\text{La}_4\text{Ni}_3\text{O}_{10}$ , we performed GGA +  $U$  calculations with  $U$  values ranging from 2 to 5 eV. Different magnetic states were targeted including ferromagnetic (FM), A-type antiferromagnetic (A-AFM), C-type antiferromagnetic (C-AFM), and G-type antiferromagnetic (G-AFM) [depicted in Fig. 5(a)]. Importantly, we also attempted a so-called M/0/M (magnetic/nonmagnetic/magnetic) state that consists of outer planes that are antiferromagnetically coupled with no moment on the inner planes (corresponding to a magnetic pattern of the six planes in the unit cell (three per trilayer) as follows:  $\uparrow, -, \downarrow; \uparrow, -, \downarrow$ , where  $-$  represents a node. Such a magnetic state was determined from the intensity distribution of the superlattice reflections derived from single-crystal neutron diffraction data taken to test for the presence of a spin density wave (SDW) concomitant with the CDW [41]. Note that the slight incommensurability of the SDW ordering vector in  $\text{La}_4\text{Ni}_3\text{O}_{10}$  results in an approximately five-period stripe in the plane [41].

Our results for the magnetic tendencies under pressure are shown in Fig. 5(b). We find that at ambient pressure, the ground state of the system is the M/0/M state consisting of in-plane ( $\pi, 0$ ) stripe order with a clear moment differentiation between inner and outer planes. While the inner planes have nearly quenched Ni moments  $\sim 0.10\mu_B$  (close to the NM state in Fig. 4), the outer planes consist of HS Ni atoms (with moments  $\sim 1.2\mu_B$ ). Importantly, the out-of-plane coupling matches that of the superlattice reflections obtained from neutrons:  $\uparrow, -, \downarrow$ . At 30 GPa, the M/0/M state is destabilized in favor of a FM state for the supercell sizes we analyzed here for  $U$  values above 4 eV, with HS Ni in both the inner and

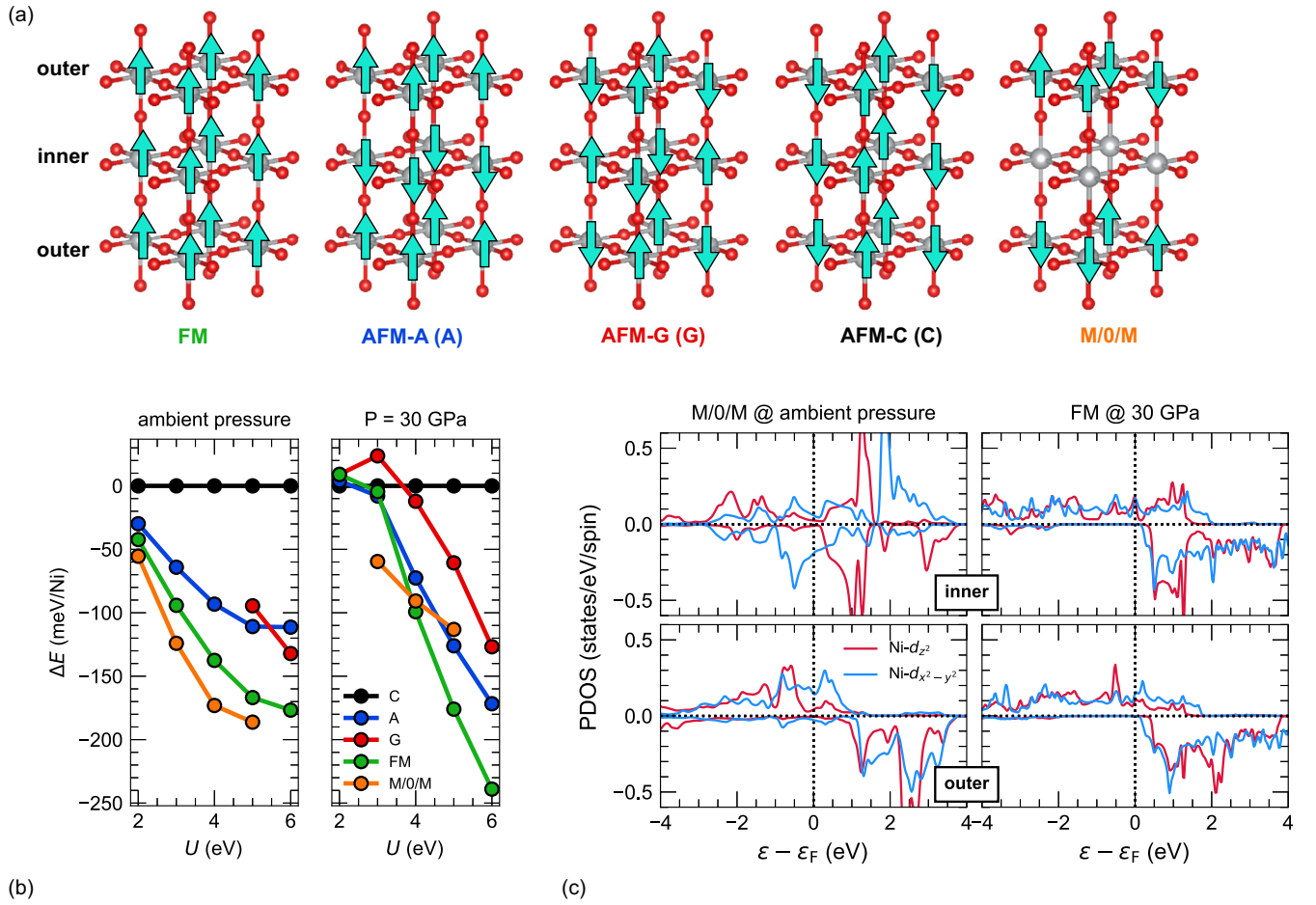


FIG. 5. Magnetic tendencies in  $\text{La}_4\text{Ni}_3\text{O}_{10}$  under pressure. (a) Different spin configurations within the trilayer unit attempted in our calculations. (b) Energy differences between different magnetic configurations at ambient pressure (left) and at 30 GPa (right). The  $C$ -AFM (C) magnetic configuration is taken as the reference. At ambient pressure, we find that the  $G$ -AFM (G) state can be converged only for large values of the Hubbard  $U$ , while for smaller values it converges to the  $C$ -type AFM solution. (c) Layer- and orbital-resolved partial density of states (PDOS) for the DFT +  $U$  ground state at ambient pressure (left) and 30 GPa (right). Positive (negative) is taken for the majority (minority) spin channel.

outer planes (with Ni moments  $\sim 1.2 \mu_B$ ). Electronically, the low-energy states are dominated by mixed Ni  $e_g$  states around the Fermi level [see Fig. 5(c)] in both the M/O/M state at ambient pressure and the FM state at high pressure, suggesting both orbitals are relevant for the low-energy physics of this material. As indicated above, the magnetic solutions we have obtained display the features of the spin states depicted in Fig. 4 (HS/LS/NM) but with orbital occupations in the Ni  $e_g$  sector that reveal some deviations with respect to those in the pure ionic limit due to the itinerant character of  $\text{La}_4\text{Ni}_3\text{O}_{10}$  (see Appendix D and Table I therein for further details).

The crucial conclusions drawn from our magnetic trends for  $\text{La}_4\text{Ni}_3\text{O}_{10}$  are as follows: (1) Both ferromagnetic and antiferromagnetic couplings can be relevant. (2) The transition between magnetic ground states with pressure is driven by a redistribution in both the  $d_{z^2}$  orbitals (which control the out-of-plane electronic structure) and the  $d_{x^2-y^2}$  orbitals (which dominate the in-plane electronic structure). This suggests that the  $d_{x^2-y^2}$  orbitals play a relevant role in the physics of  $\text{La}_4\text{Ni}_3\text{O}_{10}$ , as we observed in the bilayer material [42]. (3) The electronic structure of the inner and outer layers in the trilayer RP nickelate exhibits distinct electronic

and magnetic behavior akin to that observed in (multilayer) cuprates [43].

#### IV. SUMMARY AND CONCLUSIONS

We studied the structural, electronic, and magnetic properties of the trilayer  $\text{La}_4\text{Ni}_3\text{O}_{10}$  Ruddlesden-Popper nickelate as a function of hydrostatic pressure (and compared them with its bilayer counterpart,  $\text{La}_3\text{Ni}_2\text{O}_7$ ) from a first-principles perspective. In both materials, an orthorhombic (monoclinic)-to-tetragonal transition under pressure was found that is concomitant with the onset of superconductivity. Their electronic structures can be understood using a quantum-coupled unit, wherein  $n$  molecular subbands arise as the  $d_{z^2}$  orbitals overlap strongly along the  $c$  axis (with a bonding-antibonding complex being formed for the bilayer and a bonding-nonbonding-antibonding complex being formed for the trilayer) that are hybridized with active Ni  $d_{x^2-y^2}$  orbitals that control the electronic structure in the plane. In the nonmagnetic state, the electronic structure does not change significantly with pressure, other than the introduction of an extra pocket of  $d_{z^2}$  character at the corner of the tetragonal



zone in  $\text{La}_4\text{Ni}_3\text{O}_{10}$ . The magnetic tendencies of the trilayer RP nickelate indicate that the ground state at ambient pressure is consistent with the spin density wave model previously suggested by neutron diffraction data, with distinct inner (nonmagnetic) and stripe-ordered outer Ni layers (antiferromagnetically coupled along  $c$ ), giving rise to an overall  $\uparrow$ ,  $0$ ,  $\downarrow$  stacking. Such a state is destabilized by the pressures at which superconductivity arises. The distinct behaviors of the inner and outer planes in the trilayer RP nickelate indicate that superconductivity might arise from layer differentiation, like in multilayer cuprates.

### ACKNOWLEDGMENTS

H.L. and A.S.B. acknowledge NSF Grant No. DMR-2045826 and NSF Grant No. DMR-2323971, and the ASU Research Computing Center for HPC resources. M.R.N. was supported by the Materials Sciences and Engineering

Division, Basic Energy Sciences, Office of Science, U.S. Department of Energy.

### APPENDIX A: LATTICE DYNAMICS FOR $\text{La}_4\text{Ni}_3\text{O}_{10}$

As described in Sec. III A, RP nickelates undergo a structural transition from a lower-symmetry phase to a higher-symmetry (tetragonal) phase upon hydrostatic pressure. To understand this transition, we analyze the lattice dynamics of  $\text{La}_4\text{Ni}_3\text{O}_{10}$  in both the low-symmetry (monoclinic) and high-symmetry (tetragonal) crystal settings. Figure 6(a) shows the phonon dispersion for the monoclinic structure at ambient pressure and 10 GPa. No unstable modes are present in the phonon spectrum, indicating the crystal structure is stable. In contrast, we compare these results with the phonon spectrum for the tetragonal structure with pressure in Fig. 6(b). For the ambient pressure case, there are unstable modes at the

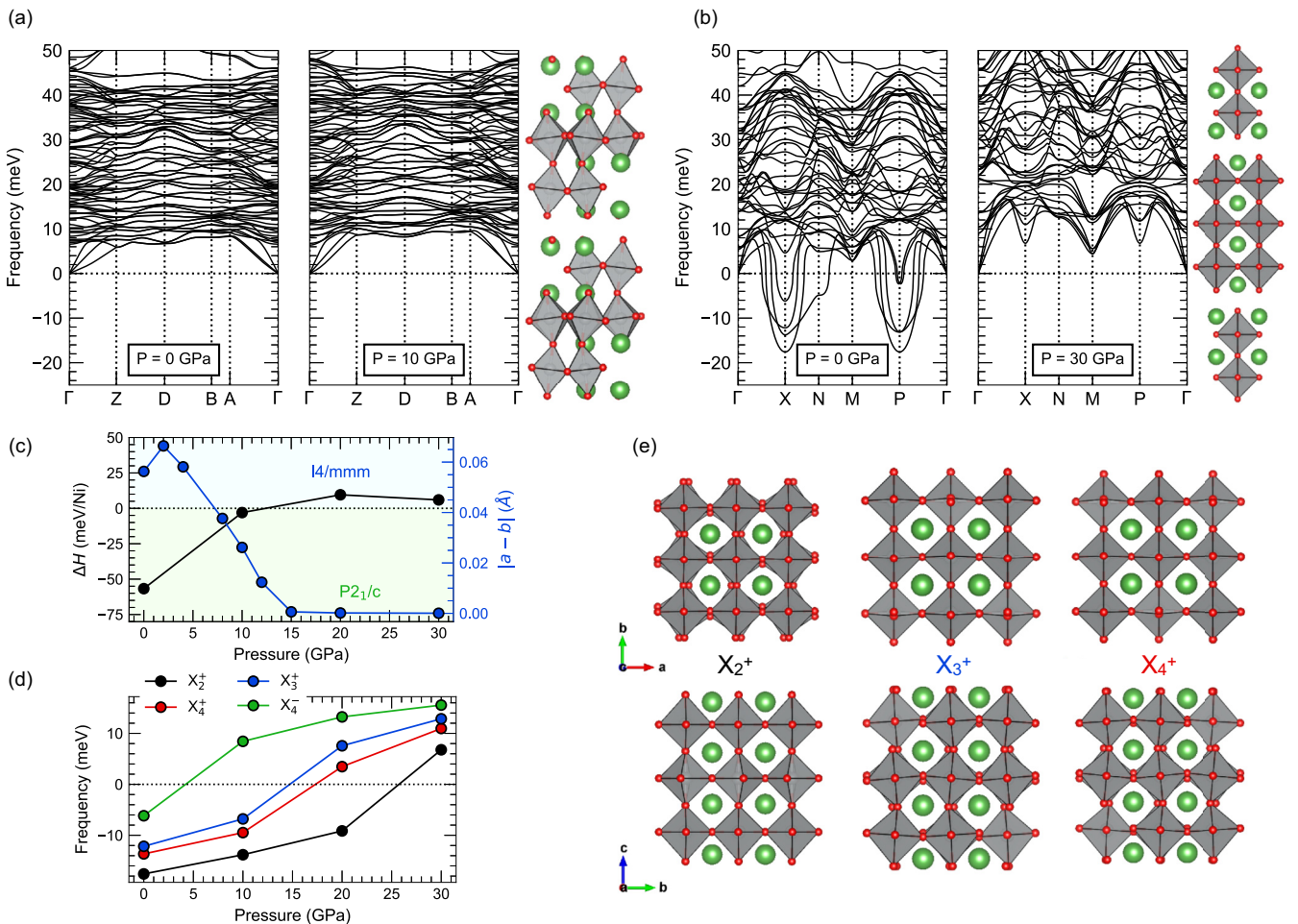


FIG. 6. Lattice dynamics of  $\text{La}_4\text{Ni}_3\text{O}_{10}$  in different crystal settings. Phonon dispersions for  $\text{La}_4\text{Ni}_3\text{O}_{10}$  along high-symmetry lines for (a) monoclinic ( $P2_1/c$ ) structure at ambient pressure (left) and 10 GPa (right) and (b) tetragonal ( $I4/mmm$ ) structure at ambient (left) and 30 GPa (right) pressures. For the monoclinic structure, high-symmetry points in the Brillouin zone correspond to  $\Gamma = (0, 0, 0)$ ,  $Z = (0.0, 0.5, 0.0)$ ,  $D = (0.0, 0.5, 0.5)$ ,  $B = (0.0, 0.0, 0.5)$ ,  $A = (-0.5, 0.0, 0.5)$ . For the tetragonal structure, high-symmetry points in the Brillouin zone correspond to  $\Gamma = (0, 0, 0)$ ,  $X = (0.0, 0.0, 0.5)$ ,  $N = (0.0, 0.5, 0.0)$ ,  $M = (0.5, 0.5, -0.5)$ , and  $P = (0.25, 0.25, 0.25)$ . (c) Enthalpy difference between the monoclinic and tetragonal structures and tetragonalization of the in-plane lattice parameters for the monoclinic structure as a function of pressure. (d) Phonons at the X point as a function of pressure. (e) Crystal distortions according to the  $X_2^+$ ,  $X_3^+$ , and  $X_4^+$  irreducible representations (irreps) of the  $I4/mmm$  space group in the  $ab$  (top) and  $bc$  (bottom) planes.

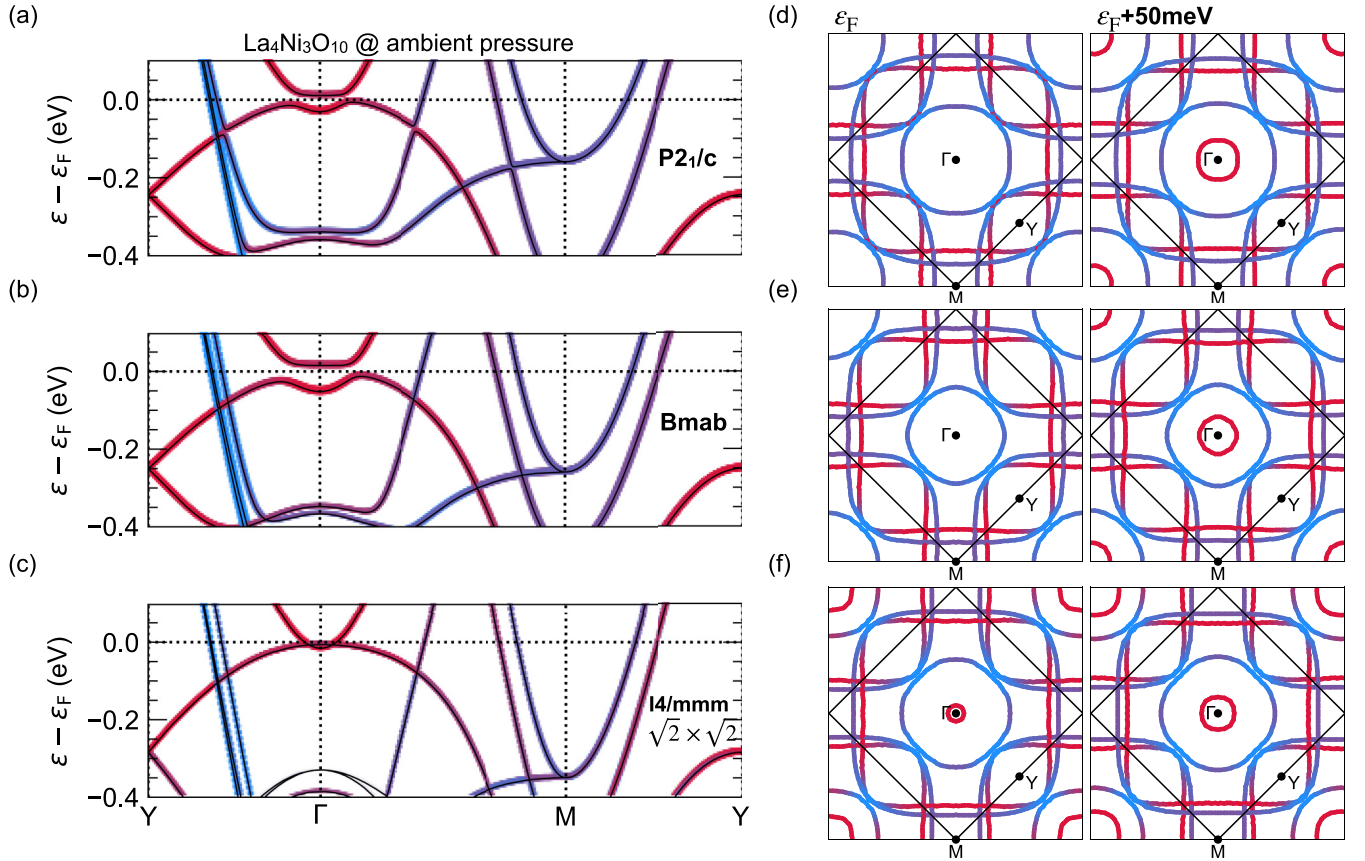


FIG. 7. Low-energy electronic structure  $\text{La}_4\text{Ni}_3\text{O}_{10}$  in different crystal settings at ambient pressure. Orbital-resolved (Ni  $e_g$ ) band structures in the (a)  $P2_1/c$ , (b)  $Bmab$ , and (c)  $I4/mmm(\sqrt{2} \times \sqrt{2})$  crystal settings. Red (blue) corresponds to Ni  $d_{z^2}$  ( $d_{x^2-y^2}$ ) orbital character. (d)–(f) Corresponding constant-energy surfaces in the  $k_z = 0$  plane at  $\varepsilon_F$  (left) and  $\varepsilon_F + 50$  meV (right).

$X$ ,  $N$ , and  $P$  points. In the main text, we focused on the  $X$  point because these modes correspond to the monoclinic distortions [see Fig. 6(e)], while the  $N$  and  $P$  points do not, based on a symmetry analysis using ISOTROPY [71]. With hydrostatic pressure, the unstable modes become quenched [see Fig. 6(d)], and we see that the  $I4/mmm$  structure becomes energetically more favored based on enthalpy differences [see Fig. 6(c)].

#### APPENDIX B: BAND STRUCTURES AND CONSTANT-ENERGY SURFACES FOR $\text{La}_4\text{Ni}_3\text{O}_{10}$ IN DIFFERENT SPACE GROUP SYMMETRIES

Figure 7 compares the computed band structure of  $\text{La}_4\text{Ni}_3\text{O}_{10}$  at ambient pressure within different crystal settings. Importantly, the monoclinic ( $P2_1/c$ ) and orthorhombic ( $Bmab$ ) crystal phases exhibit the gapped  $d_{z^2}$  band mentioned in the main text, while the tetragonal ( $I4/mmm$ ) does not. This supports our argument that the gapping is due to band folding and is not associated with the charge density wave.

We note that in the lower-symmetry structures (monoclinic and orthorhombic), the gapping of the  $d_{z^2}$  band removes the  $\gamma$  pocket from the Fermi surface. This pocket is reintroduced in the tetragonal setting where this gap is closed [or

with a small shift of the Fermi level (50 meV), as shown in Figs. 7(d)–7(f)].

#### APPENDIX C: ELECTRONIC STRUCTURE OF $\text{La}_3\text{Ni}_2\text{O}_7$

Figure 8 summarizes the paramagnetic electronic structure of  $\text{La}_3\text{Ni}_2\text{O}_7$  in the ambient pressure orthorhombic ( $Amam$ ) and high-pressure ( $P = 30$  GPa) tetragonal ( $I4/mmm$ ) structures.

As described before by us and others, focusing on the Ni  $e_g$  states near the Fermi level, the Ni  $d_{z^2}$  states are split by  $\sim 1$  eV into an occupied bonding and unoccupied antibonding combination in the ambient pressure  $Amam$  phase due to the quantum confinement provided by the nickel oxygen bilayers of the structure. The Ni  $d_{x^2-y^2}$  dispersion is large, with a bandwidth of  $\sim 2.5$  eV, and this orbital remains only partially occupied. Turning to the electronic structure at high pressure ( $P = 30$  GPa,  $Fmmm$  phase), we find that the overall electronic structure within GGA is qualitatively similar to the ambient pressure  $Amam$  phase, with some quantitative differences. The Ni  $d_{x^2-y^2}$  dispersion increases to 4 eV, and the bonding-antibonding Ni  $d_{z^2}$  splitting increases to  $\sim 1.5$  eV. Like in the ambient pressure case, the dominant density of states around the Fermi level for the nonmagnetic calculation at 29.5 GPa is that from Ni  $d_{z^2}$  orbitals, followed by that from the Ni  $d_{x^2-y^2}$  orbitals.



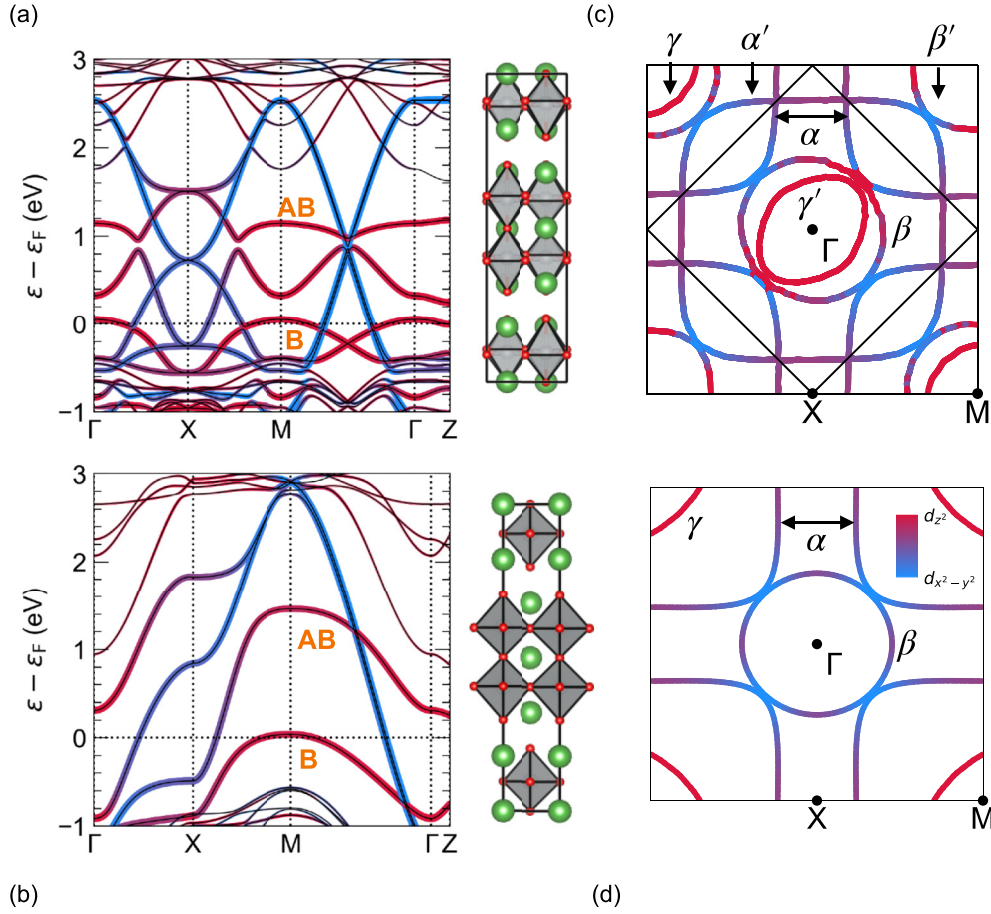


FIG. 8. Electronic structure of  $\text{La}_3\text{Ni}_2\text{O}_7$  at ambient pressure ( $A_{mm}$ , top row) and  $P = 30$  GPa ( $I4/mmm$ , bottom row). (a) and (b) Orbital-resolved band structure along high-symmetry lines highlighting the Ni  $d_{z^2}$  (red) and Ni  $d_{x^2-y^2}$  (blue) orbital characters for the ambient ( $A_{mm}$ ) and 30 GPa ( $I4/mmm$ ) phases, respectively. (c) and (d) Corresponding Fermi surfaces for (a) and (b) in the  $k_z = 0$  plane with high-symmetry points and the  $\alpha$ ,  $\beta$ , and  $\gamma$  sheets denoted. Primed ( $'$ ) sheets denote the back-folded version of the unprimed sheets for the  $A_{mm}$  case. Ni  $d_{z^2}$  bonding (B) and antibonding (AB) bands are labeled.

#### APPENDIX D: OCCUPATIONS AND MAGNETIC MOMENTS IN $\text{La}_4\text{Ni}_3\text{O}_{10}$

Table I summarizes the layer-resolved magnetic moments and Ni  $e_g$  occupations in the different magnetic configurations shown in Fig. 5. The derived spin states for the Ni atoms approximately reflect those depicted in Fig. 4, but the Ni  $e_g$

occupations do not exactly match those in the ionic limit because  $\text{La}_4\text{Ni}_3\text{O}_{10}$  is an itinerant system with dispersive  $d_{x^2-y^2}$  and  $d_{z^2}$  bands, which introduces significant deviations in occupations with respect to the pure ionic limit. In order to assign HS, LS, or NM labels in Table I, we use the derived magnetic moments from the level scheme in Fig. 4 as a guide. For high-spin Ni, a moment  $\sim 1.3\mu_B$  is expected, so we assign

TABLE I. Layer-resolved moments and  $e_g$  occupations for the Ni atoms in different magnetic states for  $\text{La}_4\text{Ni}_3\text{O}_{10}$  within GGA+ $U$  ( $U = 4$  eV,  $J_H = 0.7$  eV).

Solution (pressure)	Spin state	Layer	$ m $ (in units of $\mu_B$ )	$d_{z^2}$ (up)	$d_{z^2}$ (down)	$d_{x^2-y^2}$ (up)	$d_{x^2-y^2}$ (down)
$M/0/M$ (ambient)	NM	inner	0.10	0.58	0.33	0.37	0.71
	HS	outer	1.21	0.89	0.19	0.75	0.25
FM (30 GPa)	HS	inner	1.09	0.77	0.22	0.74	0.20
	HS	outer	1.23	0.87	0.19	0.75	0.23
A-AFM (30 GPa)	HS/LS	inner	0.97	0.79	0.29	0.64	0.22
	HS	outer	1.12	0.86	0.24	0.71	0.21
G-AFM (30 GPa)	LS/NM	inner	0.39	0.83	0.27	0.37	0.52
	LS/NM	outer	0.39	0.84	0.25	0.36	0.57
C-AFM (30 GPa)	LS	inner	0.64	0.58	0.33	0.72	0.32
	HS/LS	outer	0.91	0.84	0.22	0.65	0.36

a HS label to Ni atoms with moments close to this value. For low-spin Ni, a moment  $\sim 0.7\mu_B$  is expected [with some disproportionation between inner (lower moment) and outer (higher moment) Ni since the odd-symmetry nonbonding state has no contribution from the inner layers], so we assign a LS label to Ni atoms with moments close to this value. For some cases, the orbital occupations give rise to magnetic moments in between NM and LS, as well as in between LS and HS, so this is reflected in the assigned labels.

Note that even though the overall Ni  $e_g$  occupations within the Ni muffin-tin spheres (which contain some contribution from the oxygen tails) are close to two electrons in each case, a nominal  $d^8$  filling cannot explain the values and disproportionation in the magnetic moments we obtain. We remark that the  $e_g$  occupations we find are in agreement with many-body DFT+dynamical mean-field theory occupations [68,70], which also indicate the number of  $e_g$  electrons is approximately two.

- 
- [1] J. Bednorz and K. Müller, Possible high  $T_c$  superconductivity in the Ba-La-Cu-O system, *Z. Phys. B* **64**, 189 (1986).
- [2] D. Li, K. Lee, B. Y. Wang, M. Osada, S. Crossley, H. R. Lee, Y. Cui, Y. Hikita, and H. Y. Hwang, Superconductivity in an infinite-layer nickelate, *Nature (London)* **572**, 624 (2019).
- [3] M. Osada, B. Y. Wang, B. H. Goodge, K. Lee, H. Yoon, K. Sakuma, D. Li, M. Miura, L. F. Kourkoutis, and H. Y. Hwang, A superconducting praseodymium nickelate with infinite layer structure, *Nano Lett.* **20**, 5735 (2020).
- [4] M. Osada, B. Y. Wang, B. H. Goodge, S. P. Harvey, K. Lee, D. Li, L. F. Kourkoutis, and H. Y. Hwang, Nickelate superconductivity without rare-earth magnetism: (La, Sr)NiO<sub>2</sub>, *Adv. Mater.* **33**, 2104083 (2021).
- [5] S. Zeng, C. Li, L. E. Chow, Y. Cao, Z. Zhang, C. S. Tang, X. Yin, Z. S. Lim, J. Hu, P. Yang, and A. Ariando, Superconductivity in infinite-layer nickelate La<sub>1-x</sub>Ca<sub>x</sub>NiO<sub>2</sub> thin films, *Sci. Adv.* **8**, eabl9927 (2022).
- [6] G. A. Pan, D. F. Segedin, H. LaBollita, Q. Song, E. M. Nica, B. H. Goodge, A. T. Pierce, S. Doyle, S. Novakov, D. C. Carrizales, A. T. NDiaye, P. Shafer, H. Paik, J. T. Heron, J. A. Mason, A. Yacoby, L. F. Kourkoutis, O. Erten, C. M. Brooks, A. S. Botana *et al.*, Superconductivity in a quintuple-layer square-planar nickelate, *Nat. Mater.* **21**, 160 (2022).
- [7] H. Sun, M. Huo, X. Hu, J. Li, Z. Liu, Y. Han, L. Tang, Z. Mao, P. Yang, B. Wang, J. Cheng, D.-X. Yao, G.-M. Zhang, and M. Wang, Signatures of superconductivity near 80 K in a nickelate under high pressure, *Nature (London)* **621**, 493 (2023).
- [8] J. Hou, P.-T. Yang, Z.-Y. Liu, J.-Y. Li, P.-F. Shan, L. Ma, G. Wang, N.-N. Wang, H.-Z. Guo, J.-P. Sun, Y. Uwatoko, M. Wang, G.-M. Zhang, B.-S. Wang, and J.-G. Cheng, Emergence of high-temperature superconducting phase in pressurized La<sub>3</sub>Ni<sub>2</sub>O<sub>7</sub> crystals, *Chin. Phys. Lett.* **40**, 117302 (2023).
- [9] Y. Zhang, D. Su, Y. Huang, H. Sun, M. Huo, Z. Shan, K. Ye, Z. Yang, R. Li, M. Smidman, M. Wang, L. Jiao, and H. Yuan, High-temperature superconductivity with zero-resistance and strange metal behavior in La<sub>3</sub>Ni<sub>2</sub>O<sub>7- $\delta$</sub> , [arXiv:2307.14819](https://arxiv.org/abs/2307.14819).
- [10] Y. Zhou, J. Guo, S. Cai, H. Sun, P. Wang, J. Zhao, J. Han, X. Chen, Q. Wu, Y. Ding, M. Wang, T. Xiang, H.-kwang Mao, and L. Sun, Evidence of filamentary superconductivity in pressurized La<sub>3</sub>Ni<sub>2</sub>O<sub>7</sub> single crystals, [arXiv:2311.12361](https://arxiv.org/abs/2311.12361).
- [11] K. Chen, X. Liu, J. Jiao, M. Zou, Y. Luo, Q. Wu, N. Zhang, Y. Guo, and L. Shu, Evidence of spin density waves in La<sub>3</sub>Ni<sub>2</sub>O<sub>7- $\delta$</sub> , [arXiv:2311.15717](https://arxiv.org/abs/2311.15717).
- [12] L. Wang, Y. Li, S.-Y. Xie, F. Liu, H. Sun, C. Huang, Y. Gao, T. Nakagawa, B. Fu, B. Dong, Z. Cao, R. Yu, S. I. Kawaguchi, H. Kadobayashi, M. Wang, C. Jin, H.-K. Mao, and H. Liu, Structure responsible for the superconducting state in La<sub>3</sub>Ni<sub>2</sub>O<sub>7</sub> at high-pressure and low-temperature conditions, *J. Am. Chem. Soc.* **146**, 7506 (2024).
- [13] Y. Zhang, L.-F. Lin, A. Moreo, and E. Dagotto, Electronic structure, dimer physics, orbital-selective behavior, and magnetic tendencies in the bilayer nickelate superconductor La<sub>3</sub>Ni<sub>2</sub>O<sub>7</sub> under pressure, *Phys. Rev. B* **108**, L180510 (2023).
- [14] X. Chen, P. Jiang, J. Li, Z. Zhong, and Y. Lu, Critical charge and spin instabilities in superconducting La<sub>3</sub>Ni<sub>2</sub>O<sub>7</sub>, [arXiv:2307.07154](https://arxiv.org/abs/2307.07154).
- [15] F. Lechermann, J. Gondolf, S. Bötzel, and I. M. Eremin, Electronic correlations and superconducting instability in La<sub>3</sub>Ni<sub>2</sub>O<sub>7</sub> under high pressure, *Phys. Rev. B* **108**, L201121 (2023).
- [16] V. Christiansson, F. Petocchi, and P. Werner, Correlated electronic structure of La<sub>3</sub>Ni<sub>2</sub>O<sub>7</sub> under pressure, *Phys. Rev. Lett.* **131**, 206501 (2023).
- [17] Z. Luo, X. Hu, M. Wang, W. Wú, and D.-X. Yao, Bilayer two-orbital model of La<sub>3</sub>Ni<sub>2</sub>O<sub>7</sub> under pressure, *Phys. Rev. Lett.* **131**, 126001 (2023).
- [18] Y. Gu, C. Le, Z. Yang, X. Wu, and J. Hu, Effective model and pairing tendency in bilayer Ni-based superconductor La<sub>3</sub>Ni<sub>2</sub>O<sub>7</sub>, [arXiv:2306.07275](https://arxiv.org/abs/2306.07275).
- [19] Y. Shen, M. Qin, and G.-M. Zhang, Effective bi-layer model Hamiltonian and density-matrix renormalization group study for the high- $T_c$  superconductivity in La<sub>3</sub>Ni<sub>2</sub>O<sub>7</sub> under high pressure, *Chin. Phys. Lett.* **40**, 127401 (2023).
- [20] W. Wú, Z. Luo, D.-X. Yao, and M. Wang, Superexchange and charge transfer in the nickelate superconductor La<sub>3</sub>Ni<sub>2</sub>O<sub>7</sub> under pressure, *Sci. China: Phys., Mech. Astron.* **67**, 117402 (2024).
- [21] Q.-G. Yang, D. Wang, and Q.-H. Wang, Possible  $s_{\pm}$ -wave superconductivity in La<sub>3</sub>Ni<sub>2</sub>O<sub>7</sub>, *Phys. Rev. B* **108**, L140505 (2023).
- [22] Y.-B. Liu, J.-W. Mei, F. Ye, W.-Q. Chen, and F. Yang,  $s^{\pm}$ -wave pairing and the destructive role of apical-oxygen deficiencies in La<sub>3</sub>Ni<sub>2</sub>O<sub>7</sub> under pressure, *Phys. Rev. Lett.* **131**, 236002 (2023).
- [23] Y. Zhang, L.-F. Lin, A. Moreo, T. A. Maier, and E. Dagotto, Structural phase transition,  $s_{\pm}$ -wave pairing, and magnetic stripe order in bilayered superconductor La<sub>3</sub>Ni<sub>2</sub>O<sub>7</sub> under pressure, *Nat. Commun.* **15**, 2470 (2024).
- [24] X.-Z. Qu, D.-W. Qu, J. Chen, C. Wu, F. Yang, W. Li, and G. Su, Bilayer  $t$ - $J$ - $J_{\perp}$  model and magnetically mediated pairing in the pressurized nickelate La<sub>3</sub>Ni<sub>2</sub>O<sub>7</sub>, *Phys. Rev. Lett.* **132**, 036502 (2024).
- [25] Y.-F. Yang, G.-M. Zhang, and F.-C. Zhang, Interlayer valence bonds and two-component theory for high- $T_c$  superconductivity of La<sub>3</sub>Ni<sub>2</sub>O<sub>7</sub> under pressure, *Phys. Rev. B* **108**, L201108 (2023).

- [26] Y. Zhang, L.-F. Lin, A. Moreo, T. A. Maier, and E. Dagotto, Trends in electronic structures and  $s_{\pm}$ -wave pairing for the rare-earth series in bilayer nickelate superconductor  $R_3Ni_2O_7$ , *Phys. Rev. B* **108**, 165141 (2023).
- [27] D.-C. Lu, M. Li, Z.-Y. Zeng, W. Hou, J. Wang, F. Yang, and Y.-Z. You, Superconductivity from doping symmetric mass generation insulators: Application to  $La_3Ni_2O_7$  under pressure, [arXiv:2308.11195](https://arxiv.org/abs/2308.11195).
- [28] Y.-H. Tian, Y. Chen, J.-M. Wang, R.-Q. He, and Z.-Y. Lu, Correlation effects and concomitant two-orbital  $s_{\pm}$ -wave superconductivity in  $La_3Ni_2O_7$  under high pressure, [arXiv:2308.09698](https://arxiv.org/abs/2308.09698).
- [29] J. Huang, Z. D. Wang, and T. Zhou, Impurity and vortex states in the bilayer high-temperature superconductor  $La_3Ni_2O_7$ , *Phys. Rev. B* **108**, 174501 (2023).
- [30] R. Jiang, J. Hou, Z. Fan, Z.-J. Lang, and W. Ku, Pressure driven fractionalization of ionic spins results in cupratelike high- $T_c$  superconductivity in  $La_3Ni_2O_7$ , *Phys. Rev. Lett.* **132**, 126503 (2024).
- [31] Z. Liao, L. Chen, G. Duan, Y. Wang, C. Liu, R. Yu, and Q. Si, Electron correlations and superconductivity in  $La_3Ni_2O_7$  under pressure tuning, *Phys. Rev. B* **108**, 214522 (2023).
- [32] C. Lu, Z. Pan, F. Yang, and C. Wu, Interlayer-coupling-driven high-temperature superconductivity in  $La_3Ni_2O_7$  under pressure, *Phys. Rev. Lett.* **132**, 146002 (2024).
- [33] H. Oh and Y.-H. Zhang, Type-II  $t - J$  model and shared superexchange coupling from Hund's rule in superconducting  $La_3Ni_2O_7$ , *Phys. Rev. B* **108**, 174511 (2023).
- [34] Q. Qin and Y.-F. Yang, High- $T_c$  superconductivity by mobilizing local spin singlets and possible route to higher  $T_c$  in pressurized  $La_3Ni_2O_7$ , *Phys. Rev. B* **108**, L140504 (2023).
- [35] H. Sakakibara, N. Kitamine, M. Ochi, and K. Kuroki, Possible high  $T_c$  superconductivity in  $La_3Ni_2O_7$  under high pressure through manifestation of a nearly half-filled bilayer Hubbard model, *Phys. Rev. Lett.* **132**, 106002 (2024).
- [36] D. A. Shilenko and I. V. Leonov, Correlated electronic structure, orbital-selective behavior, and magnetic correlations in double-layer  $La_3Ni_2O_7$  under pressure, *Phys. Rev. B* **108**, 125105 (2023).
- [37] H. Sakakibara, M. Ochi, H. Nagata, Y. Ueki, H. Sakurai, R. Matsumoto, K. Terashima, K. Hirose, H. Ohta, M. Kato, Y. Takano, and K. Kuroki, Theoretical analysis on the possibility of superconductivity in the trilayer Ruddlesden-Popper nickelate  $La_4Ni_3O_{10}$  under pressure and its experimental examination: Comparison with  $La_3Ni_2O_7$ , *Phys. Rev. B* **109**, 144511 (2024).
- [38] Q. Li, Y.-J. Zhang, Z.-N. Xiang, Y. Zhang, X. Zhu, and H.-H. Wen, Signature of superconductivity in pressurized  $La_4Ni_3O_{10}$ , *Chin. Phys. Lett.* **41**, 017401 (2024).
- [39] M. Zhang, C. Pei, X. Du, W. Hu, Y. Cao, Q. Wang, J. Wu, Y. Li, H. Liu, C. Wen, Y. Zhao, C. Li, W. Cao, S. Zhu, Q. Zhang, N. Yu, P. Cheng, L. Zhang, Z. Li, J. Zhao *et al.*, Superconductivity in trilayer nickelate  $La_4Ni_3O_{10}$  under pressure, [arXiv:2311.07423](https://arxiv.org/abs/2311.07423).
- [40] Y. Zhu, E. Zhang, B. Pan, X. Chen, D. Peng, L. Chen, H. Ren, F. Liu, N. Li, Z. Xing, J. Han, J. Wang, D. Jia, H. Wo, Y. Gu, Y. Gu, L. Ji, W. Wang, H. Gou, Y. Shen, T. Ying *et al.*, Superconductivity in trilayer nickelate  $La_4Ni_3O_{10}$  single crystals, [arXiv:2311.07353](https://arxiv.org/abs/2311.07353).
- [41] J. Zhang, D. Phelan, A. S. Botana, Y.-S. Chen, H. Zheng, M. Krogstad, S. G. Wang, Y. Qiu, J. A. Rodriguez-Rivera, R. Osborn, S. Rosenkranz, M. R. Norman, and J. F. Mitchell, Intertwined density waves in a metallic nickelate, *Nat. Commun.* **11**, 6003 (2020).
- [42] H. LaBollita, V. Pardo, M. R. Norman, and A. S. Botana, Electronic structure and magnetic properties of  $La_3Ni_2O_7$  under pressure: active role of the Ni- $d_{x^2-y^2}$  orbitals, [arXiv:2309.17279](https://arxiv.org/abs/2309.17279).
- [43] H. Mukuda, S. Shimizu, A. Iyo, and Y. Kitaoka, High- $T_c$  superconductivity and antiferromagnetism in multilayered copper oxides – A new paradigm of superconducting mechanism–, *J. Phys. Soc. Jpn.* **81**, 011008 (2012).
- [44] P. Hohenberg and W. Kohn, Inhomogeneous electron gas, *Phys. Rev.* **136**, B864 (1964).
- [45] W. Kohn and L. J. Sham, Self-consistent equations including exchange and correlation effects, *Phys. Rev.* **140**, A1133 (1965).
- [46] J. Zhang, H. Zheng, Y.-S. Chen, Y. Ren, M. Yonemura, A. Huq, and J. F. Mitchell, High oxygen pressure floating zone growth and crystal structure of the metallic nickelates  $R_4Ni_3O_{10}$  ( $R = La, Pr$ ), *Phys. Rev. Mater.* **4**, 083402 (2020).
- [47] M.-C. Jung, J. Kapeghian, C. Hanson, B. Pamuk, and A. S. Botana, Electronic structure of higher-order Ruddlesden-Popper nickelates, *Phys. Rev. B* **105**, 085150 (2022).
- [48] G. Kresse and J. Hafner, *Ab initio* molecular dynamics for liquid metals, *Phys. Rev. B* **47**, 558(R) (1993).
- [49] G. Kresse and D. Joubert, From ultrasoft pseudopotentials to the projector augmented-wave method, *Phys. Rev. B* **59**, 1758 (1999).
- [50] G. Kresse and J. Furthmüller, Efficient iterative schemes for *ab initio* total-energy calculations using a plane-wave basis set, *Phys. Rev. B* **54**, 11169 (1996).
- [51] J. P. Perdew, K. Burke, and M. Ernzerhof, Generalized gradient approximation made simple, *Phys. Rev. Lett.* **77**, 3865 (1996).
- [52] A. Togo and I. Tanaka, First principles phonon calculations in materials science, *Scr. Mater.* **108**, 1 (2015).
- [53] P. Blaha, K. Schwarz, F. Tran, R. Laskowski, G. K. H. Madsen, and L. D. Marks, WIEN2k: An APW+lo program for calculating the properties of solids, *J. Chem. Phys.* **152**, 074101 (2020).
- [54] M. T. Czyżyk and G. A. Sawatzky, Local-density functional and on-site correlations: The electronic structure of  $La_2CuO_4$  and  $LaCuO_3$ , *Phys. Rev. B* **49**, 14211 (1994).
- [55] J. Zhang, A. S. Botana, J. W. Freeland, D. Phelan, H. Zheng, V. Pardo, M. R. Norman, and J. F. Mitchell, Large orbital polarization in a metallic square-planar nickelate, *Nat. Phys.* **13**, 864 (2017).
- [56] J. Krishna, H. LaBollita, A. O. Fumega, V. Pardo, and A. S. Botana, Effects of Sr doping on the electronic and spin-state properties of infinite-layer nickelates: Nature of holes, *Phys. Rev. B* **102**, 224506 (2020).
- [57] A. S. Botana, V. Pardo, W. E. Pickett, and M. R. Norman, Charge ordering in  $Ni^{1+}/Ni^{2+}$  nickelates:  $La_4Ni_3O_8$  and  $La_3Ni_2O_6$ , *Phys. Rev. B* **94**, 081105(R) (2016).
- [58] A. S. Botana, V. Pardo, and M. R. Norman, Electron doped layered nickelates: Spanning the phase diagram of the cuprates, *Phys. Rev. Mater.* **1**, 021801(R) (2017).
- [59] V. Pardo and W. E. Pickett, Pressure-induced metal-insulator and spin-state transition in low-valence layered nickelates, *Phys. Rev. B* **85**, 045111 (2012).



- [60] D. Orobengoa, C. Capillas, M. I. Aroyo, and J. M. Perez-Mato, *AMPLIMODES*: Symmetry-mode analysis on the Bilbao Crystallographic Server, *J. Appl. Crystallogr.* **42**, 820 (2009).
- [61] J. M. Perez-Mato, D. Orobengoa, and M. I. Aroyo, Mode crystallography of distorted structures, *Acta Crystallogr., Sect. A* **66**, 558 (2010).
- [62] B. Geisler, J. J. Hamlin, G. R. Stewart, R. G. Hennig, and P. J. Hirschfeld, Structural transitions, octahedral rotations, and electronic properties of  $A_3Ni_2O_7$  rare-earth nickelates under high pressure, [arXiv:2309.15078](https://arxiv.org/abs/2309.15078).
- [63] Further ambiguity has been introduced with the report of  $La_3Ni_2O_7$  with a “1313” stacking sequence of single and trilayer nickel planes [72,73]. Here, we study only the bilayer nickelate in the conventional (“2222”) stacking and leave the comparison to the alternate stacking for future work.
- [64] H. Li, X. Zhou, T. Nummy, J. Zhang, V. Pardo, W. E. Pickett, J. F. Mitchell, and D. S. Dessau, Fermiology and electron dynamics of trilayer nickelate  $La_4Ni_3O_{10}$ , *Nat. Commun.* **8**, 704 (2017).
- [65] D. Puggioni and J. M. Rondinelli, Crystal structure stability and electronic properties of the layered nickelate  $La_4Ni_3O_{10}$ , *Phys. Rev. B* **97**, 115116 (2018).
- [66] J. Li, C.-Q. Chen, C. Huang, Y. Han, M. Huo, X. Huang, P. Ma, Z. Qiu, J. Chen, X. Hu, L. Chen, T. Xie, B. Shen, H. Sun, D.-X. Yao, and M. Wang, Structural transition, electric transport, and electronic structures in the compressed trilayer nickelate  $La_4Ni_3O_{10}$ , *Sci. China: Phys., Mech. Astron.* **67**, 117403 (2024).
- [67] V. Pardo and W. E. Pickett, Quantum confinement induced molecular correlated insulating state in  $La_4Ni_3O_8$ , *Phys. Rev. Lett.* **105**, 266402 (2010).
- [68] I. V. Leonov, Electronic structure and magnetic correlations in trilayer nickelate superconductor  $La_4Ni_3O_{10}$  under pressure, [arXiv:2401.07350](https://arxiv.org/abs/2401.07350).
- [69] P.-F. Tian, H.-T. Ma, X. Ming, X.-J. Zheng, and H. Li, Effective model and electron correlations in trilayer nickelate superconductor  $La_4Ni_3O_{10}$ , [arXiv:2402.02351](https://arxiv.org/abs/2402.02351).
- [70] J.-X. Wang, Z. Ouyang, R.-Q. He, and Z.-Y. Lu, Non-Fermi liquid and Hund correlation in  $La_4Ni_3O_{10}$  under high pressure, [arXiv:2402.02581](https://arxiv.org/abs/2402.02581).
- [71] H. T. Stokes, D. M. Hatch, B. J. Campbell, and D. E. Tanner, *ISODISPLACE*: a web-based tool for exploring structural distortions, *J. Appl. Crystallogr.* **39**, 607 (2006).
- [72] X. Chen, J. Zhang, A. S. Thind, S. Sharma, H. LaBollita, G. Peterson, H. Zheng, D. Phelan, A. S. Botana, R. F. Klie, and J. F. Mitchell, Polymorphism in Ruddlesden-Popper  $La_3Ni_2O_7$ : Discovery of a hidden phase with distinctive layer stacking, *J. Am. Chem. Soc.* **146**, 3640 (2024).
- [73] P. Puphal, P. Reiss, N. Enderlein, Y.-M. Wu, G. Khaliullin, V. Sundaramurthy, T. Priessnitz, M. Knauff, L. Richter, M. Isobe, P. A. van Aken, H. Takagi, B. Keimer, Y. E. Suyolcu, B. Wehinger, P. Hansmann, and M. Hepting, Unconventional crystal structure of the high-pressure superconductor  $La_3Ni_2O_7$ , [arXiv:2312.07341](https://arxiv.org/abs/2312.07341).